CrossMark

ORIGINAL PAPER

Relationship Between Nanoindentation and Wear Properties of Stainless Steel-Reinforced Aluminium Matrix Composite

Ridvan Gecu[1] · Ahmet Karaaslan[1]

Abstract 304 Stainless steel (SS)-reinforced A356 aluminium matrix composites were manufactured by melt infiltration casting. Recycled SS shavings were pressed to obtain porous monoblock preform, and molten Al alloy was infiltrated into vacancies of the preform during casting process. Various preform preheating times (0–60 min) before casting were studied, and the effect of preheating time on relationship between nanoindentation and wear properties of produced composites was discussed. All casting operations were carried out at 730 °C. Fabricated composites were characterized by optical microscope, SEM, FEG-SEM, XRD, EDS, nanoindentation tester and ball-on-disc type tribometer with using Al_2O_3 ball as counterpart. θ-Fe_4Al_{13} and η-Fe_2Al_5 phases were obtained at the interfaces, except for 60 min preheated sample. These reaction phases increased the hardness, compressive residual stress and consequently wear resistance. On the other hand, when the sample was not preheated or preheated excessively, interface bonding was weakened and crack propagation was occurred. Cracked particles from interfacial phases in these specimens participated wear process and caused increase in wear rate of manufactured composites.

Keywords Aluminium matrix composite · Melt infiltration casting · Nanoindentation · Wear · Residual stress

1 Introduction

When developing new materials and new manufacturing technologies in the automotive industry, fuel economy, reduction in emissions and ensuring vehicle safety with competitive costs are taken as basis. The increasing need for lightweight constructions is the result of these concerns, and aluminium alloys are especially preferred to meet this requirement due to their low density, low thermal expansion, good corrosion resistance and ease of production [1]. On the other hand, considering applications that involve sliding contacts, Al alloys without reinforcing show poor strength. Instead of monolithic Al alloys, Al matrix composites (AMCs) have been widely used by various companies to manufacture automobile components such as engine pistons, disc rotor brakes, cylinder heads, drive shafts, engine blocks and connecting rods [2]. Most commonly used reinforcement materials to strengthen Al matrix for these components are ceramics owing to their high strength/density ratio, high hardness and good wear resistance [3]. However, ceramic reinforcements like SiC [4], Al_2O_3 [5], B_4C [6], TiC [7] and graphite [8] destroy the original ductility and toughness of Al matrix when they participated composite structure. Undesirable phase transformations and wetting problems at the reinforcement–matrix interface are also crucial disadvantages that cannot be fully solved yet [9].

Metal reinforcement usage in AMCs has enormous potential to compensate the detrimental effects of ceramic particles without losing competitive properties. Although low-cost environmentally friendly production of metal-reinforced AMCs is possible by using recycled products and suitable casting methods, metal reinforcement use still remains limited in Al matrix. Steel-based reinforcements come to the forefront to improve mechanical and tribological features of Al matrix in recent years. Sarkari Khorrami et al. [10]

✉ Ridvan Gecu
ridvangecu@gmail.com

[1] Department of Metallurgical and Materials Engineering, Yildiz Technical University, Istanbul, Turkey

researched in situ AMCs reinforced with Fe particles and stated that proper metallurgical bonding between Al and Fe along with outstanding mechanical features was achieved by intermetallic compound (IMC) formation at the interface. Baron et al. [11] studied both unalloyed steel (UAS) and stainless steel (SS)-reinforced AMCs and reported that tensile strength of the manufactured composites was directly related to volume fraction of the IMC at the interface. IMC increased tensile strength by generating strong bond between Al and SS while the same compound weakened bonding at Al-UAS interface and decrease mechanical properties due to its excessive amounts in microstructure. Selvakumar et al. [12] produced AA6082 matrix composite reinforced with 316L SS particles by avoiding IMC formation at the interface and confirmed improvement in composite ductility with metal reinforcements by comparison with TiC-reinforced AA6082 matrix composite fabricated by Thangarasu et al. [13]. It should be noted that tensile strength of Baron et al.'s work was much higher than that of Selvakumar et al.'s work owing to existence of IMC at the interface.

While mechanical features (ultimate tensile strength, microhardness, fatigue life and bending strength) of AMCs with metal reinforcements have been studied in a limited number, their tribological properties have not been taken into account as much as ceramic reinforcements. It is well-known fact that reinforcement influences wear rate either negatively or positively depending upon its type, distribution, particle size and volume fraction. Various wear test conditions also change wear mechanism that composite structure is exposed [14]. It is understood from this perspective that more tribological work is required to fully comprehend the wear features and their relations to mechanical properties of metal-reinforced AMCs. Several studies [15–18] on other subjects rather than composites demonstrate the hardness–wear relationship, and all of them pointed out that increasing hardness provides increase in wear resistance with one exception. In Tang et al.'s work [15], which includes this exception, the brittleness of the hardest sample causes to decrease in wear resistance and also converted dominated wear mechanism from adhesion to delamination. It can be inferred that there should be an upper limit for hardness to improve wear resistance.

Although AMCs can be manufactured in a variety of ways, the cheapest methods generally consist of molten metal routes, given the cost of production. Melt infiltration casting is a type of molten metal process that allows composite production at high reinforcement ratios up to 75%,

even under pressureless conditions thanks to vacuum supported casting technique [19, 20]. In the case of such high reinforcement ratios, the preference of Al alloy that hold the reinforcement phase together and transfer the applied load without failure becomes more important. Considering the infiltration of molten Al into narrow preform vacancies during casting process, A356 cast alloy seems the best choice as a matrix material due to its remarkable fluidity and castability properties. In material selection, corrosion features should also not be ignored because the common effects of corrosion and wear may cause dramatic increase in material weight losses [21]. Due to its excellent corrosion resistance by means of high Cr content, 304 SS alloy was selected as a reinforcement for composite production.

In this study, 304 SS-reinforced A356 matrix composites produced in a low-cost environmentally friendly way by melt infiltration casting were investigated. Relationship between nanoindentation and wear properties of manufactured composites was discussed as functions of preform preheating times and formed IMCs at the interface.

2 Experimental Procedure

A356 Al alloy was selected as matrix material because of its striking pourability characteristics, in addition to its area of use in automotive industry. Inadequacies of mechanical and tribological properties of Al alloy were enhanced by 304 SS addition. Chemical compositions of experimented alloys were reported in Table 1. Melt infiltration casting of 304 SS-reinforced A356 matrix composites was taken place in three stages including mould making, casting and characterization of final product.

2.1 Mould Making

Wax pattern with the dimensions of 25 mm in diameter and 50 mm in height is obtained by casting of molten wax into cylindrical plastic mould at 85 °C. 500 g investment powder was mixed with 200 g water for 3 min to prepare castable plaster slurry. Excessive water use results in a weak mould while excessive powder use makes mould surfaces too coarse. Also, too much mixing time causes to create lumps and becloud mechanical mixing. As consequences, water/powder ratio and mixing time were specified as 40% and 3 min to attain perfect slurry, respectively [22]. Wax pattern was settled in SS perforated flask, and prepared slurry

Table 1 Chemical compositions of A356 Al and 304 SS alloys (wt%)

Alloy	C	Si	Mn	Cr	Mg	Cu	Zn	Ni	Ti	Fe	Al
A356	–	7.0	0.1	–	0.35	0.2	0.1	–	0.2	0.2	Bal.
304 SS	0.08	1.0	2.0	18.0	–	–	–	8.0	–	Bal.	–

was cast into the flask under vibration until the pattern was all covered. The purpose of using a perforated flask is to provide plaster mould vacuuming capability. After 15 min vibrating, perforated flask was held in undisturbed condition for 2 h to harden the mould. Mould cavity was obtained by dewaxing process which was performed at 110 °C for 1 h in drying oven. Dewaxed mould in perforated flask was heated up to 700 °C gradually to provide dehydrating mould and eliminating residual wax carbon. In the first step of burnout process, flask was heated slowly to 250 °C. Water as moisture that chemically combined with investment powder turned to steam and escaped through the mould pores at this temperature. If flask was heated quickly, vapour pressure could initiate cracks in the mould. In the second step, flask was heated to 550 °C where the residual wax transformed to black carbon powder. This carbon was completely eliminated at 700 °C by forming CO and CO_2 with oxygen of the air. Burnout regime of the plaster mould was illustrated in Fig. 1.

2.2 Casting

304 SS shavings with nearly same sizes were obtained from turning machine and pressed under 220 MPa to get porous monoblock preform with the dimensions of 20 mm in diameter and 10 mm in height. 220 MPa pressure allows to get preform with 50% porosity by volume. This result was achieved by trial and error method and repeated experiments. When SS shavings were pressed under 220 MPa pressure, the density of SS preforms was measured approximately 50% of its theoretical density. The rest 50% of the preform is porosity that will be infiltrated by A356 alloy during casting. Produced preforms were inserted into mould before casting for several times (0, 10, 30 and 60 min) at the end of the burnout process. Preheating provides avoiding rapid solidification of
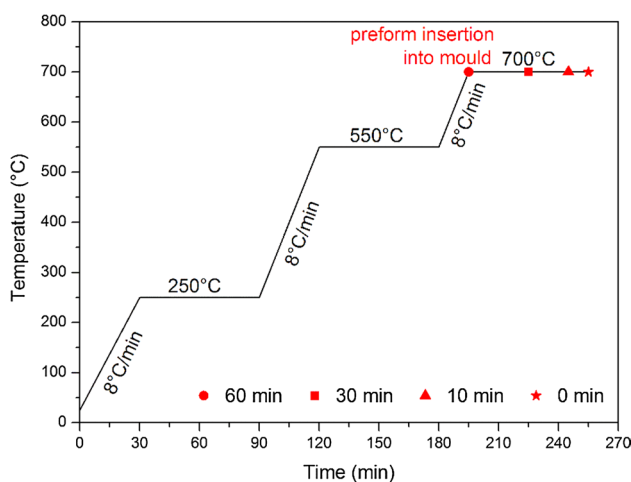
molten Al and consequently increasing the interaction time between solid 304 and liquid A356 alloys.

Schematic illustration of melt infiltration casting is shown in Fig. 2. When burnout process was completed, perforated flask with preform inside was taken out from furnace and settled in the vacuum chamber. A356 alloy melt in a clay/graphite crucible at 730 °C was poured into the flask and held there for 20 min under -10^5 Pa vacuum pressure. During this time, A356 alloy was infiltrated into SS preform vacancies. After complete solidification, mould was quenched and composite was taken out. Casting parameters were kept constant for all samples, except preform preheating times. Manufactured composites consist of A356 and 304 SS alloys at the ratio of 50% by volume.

2.3 Characterization of Final Product

Cross sections of produced composites were embedded in a cold resin. After preparation of samples by grinding and polishing, metallographic examinations of them were carried out using field emission gun scanning electron microscope (FEG-SEM, JEOL JSM 6335F) and optical microscope (OM, Nikon Eclipse MA100). Formed phases were determined by X-ray diffraction (XRD, Philips PW 3710) using CuKα radiation over 2θ range of 10°–90°. Energy-dispersive X-ray spectroscopy (EDS) analysis via FEG-SEM and scanning electron microscope (SEM, JEOL JSM 6060) was carried out to get elemental contents in specific areas and lines. After microstructural analysis, samples were subjected to wear tests by ball-on-disc type tribometer using Al_2O_3 ball with 6 mm diameter as counterpart. 10 N load was applied to polished sample surfaces with the approximate roughness of $R_a = 0.45$ μm during 100 m sliding distance with the velocity of 0.1 m/s and the stroke

Fig. 1 Burnout regime of plaster mould
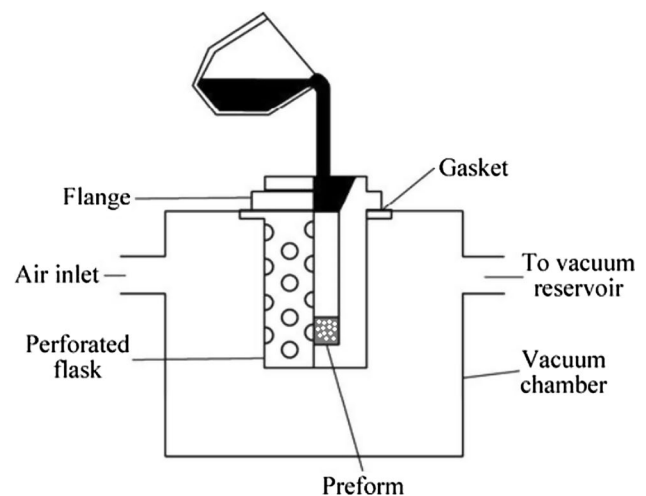
Fig. 2 Illustration of melt infiltration casting [23]

length of 6 mm in accordance with ASTM G99-17. Wear tests were carried out at 24 °C in 40% relative humidity in ambient conditions. Three tests were performed under same conditions for each sample and mean results were given with the standard deviations. Volume losses were calculated by dividing mass losses by composite density in accordance with ASTM G99-17. To ensure that obtained results were reliable,

$$W_R = \frac{V}{LP} \tag{1}$$

formula was used to calculate wear rate where W_R is wear rate, V is volume loss, L is sliding distance, and P is applied load. Volume losses were separately computed for wear tracks and mass losses. The heights and the widths of the tracks were measured by profilometer (Mahr S2) and image analyzer software (Zeiss), respectively. Both heights and widths were calculated at 4 different profiles (left, right, top and bottom sides of the wear tracks) for each specimen and mean values of these several profiles were taken into account. Calculated values were multiplied by each other and the length of the wear tracks to determine volume losses. Wear rates were given as an average of both measuring methods. All samples were examined by SEM after wear tests to study on worn surfaces.

Hardness and residual stress of composites were determined by nanoindentation test device (CSM NHT, SN06-177) equipped with a Berkovich diamond tip. Each phase for all specimens was indented at random spots at least ten times with an applied load of 100 mN in 120 steps with the interval of 1 s, and the average hardness values were calculated. Nanoindentation test device software uses Oliver and Pharr nonlinear curve fit method [24] to calculate hardness. Residual stress measurements were carried out according to Wang et al.'s work [25] using load–penetration depth (P–h) curves that nanoindentation tester records. In Wang et al.'s model, residual stress was calculated according to

$$\sigma_{res} = \frac{P_1 - P_2}{2\pi \tan^2 \alpha h_r^2} \tag{2}$$

formula where σ_{res} is the residual stress, P_1 is the maximum load of stressed sample, P_2 is the intersection of unloading of stressed sample and loading of stress-free sample, and h_r is the depth of unloading of stressed sample where load equals zero. α can be considered as geometric correction factor for sharp indenters, and it represents cone semi-angle. In this work, Berkovich indenter was used and α value for Berkovich is 65.3°. Figure 3 shows the representative load–depth curves of specimens with and without stresses. The loading and unloading curves of stressed specimen and the loading curve of the stress-free specimen should be considered to determine residual stress by Wang et al.'s model.
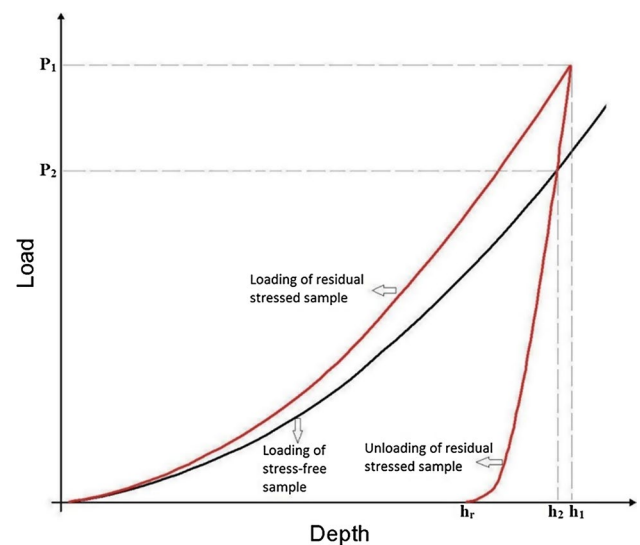
Fig. 3 Indentation load–depth curves for the samples with and without stresses
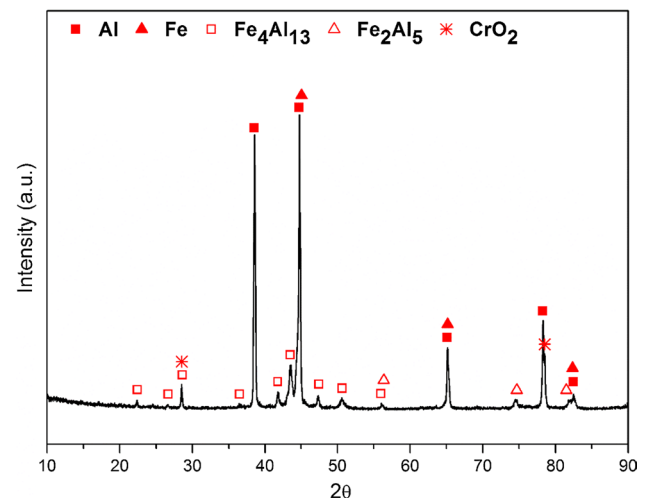
Fig. 4 XRD results of 10 min preheated 304 SS-reinforced A356 matrix composite

3 Results and Discussion

3.1 XRD Analysis

Formed phases of 304 SS-reinforced A356 matrix composites were determined by XRD analysis. Figure 4 shows X-ray diffractograms from the cross section of 10 min preheated sample. The Joint Committee on Powder Diffraction Standards (JCPDS) database was taken as basis to classify attained reflexes. XRD analysis results demonstrate that Al, Fe, θ-Fe_4Al_{13} and η-Fe_2Al_5 phases were formed as a result of Al/steel interaction during melt infiltration casting. CrO_2

phase was naturally formed on all sample surfaces after production because of the disposition of SS structures. According to Fe–Al phase diagram [26], when Al in liquid state interacts with Fe for a sufficient time, the first formed phase is θ and the second formed phase is η. If there was more interaction time, $FeAl_2$ formation would also occur but apparently, Al had completely solidified before $FeAl_2$ was formed. It seems that XRD results are in agreement with Fe–Al phase diagram.

3.2 Microstructure

Low-magnification and high-magnification secondary electron images (SEI) via FEG-SEM of 30 min preheated samples are given in Fig. 5. High-magnification image includes three regions that EDS analysis was taken. Overall morphology of manufactured composites is demonstrated in Fig. 5a. Although some casting defects at some interfaces were clearly visible, when all composite structure was taken into account, it can be said that good metallurgical and mechanical bonding were occurred. Dark regions point out A356 alloy, while light regions refer 304 SS reinforcement. The lighter tones on Al region show the chemical composition differences. Since heavier elements appear lighter in SEI, regions containing Si seem lighter in colour. The microstructure of A356 alloy intrinsically involves α-Al and eutectic (α-Al + Si) phases. It can be concluded that lighter tones on Al side indicate eutectic structure.

Double-layered interfacial phases were identified by EDS analysis, and results are reported in Table 2. Region 1 comprises more Al and less Fe than that of region 2. Results of region 3 reveal that no Al diffusion into SS occurred during infiltration. This area consists of the elements that only chemical composition of 304 SS includes. In other words, Al diffusion was limited to reaction phase formation at the interface. Considering EDS results and Al–Fe phase diagram together, θ should be adjacent to Al matrix due to its higher Al amount and η must be next to SS side owing to its higher Fe content. Formed reaction phases were marked in Fig. 5b. Another point that needs to be addressed is Si distribution in θ and η layers. Si tends to accumulate into θ instead of diffuse in η phase. It can be inferred from EDS results that η layer practically acts as a barrier to diffusion of Si atoms.

Figure 6 shows the micrographs of all produced composites with various preform preheating times taken by OM. By contrast with FEG-SEM images, light areas refer Al zone while dark regions state SS part. All phases formed during infiltration process are demonstrated in Fig. 6b. Double-layered reaction phases called as θ and η were formed in 0, 10 and 30 min preheated specimens (Fig. 6a–c), whereas only monolayer θ was obtained in 60 min preheated sample (Fig. 6d). Too much interaction between SS preform surface and oxygen in the furnace during preheating caused CrO_2 formation and its rapid growth. Grown CrO_2 film on SS surface inhibited Al infiltration into preform vacancies and consequently weakened matrix–reinforcement interaction.
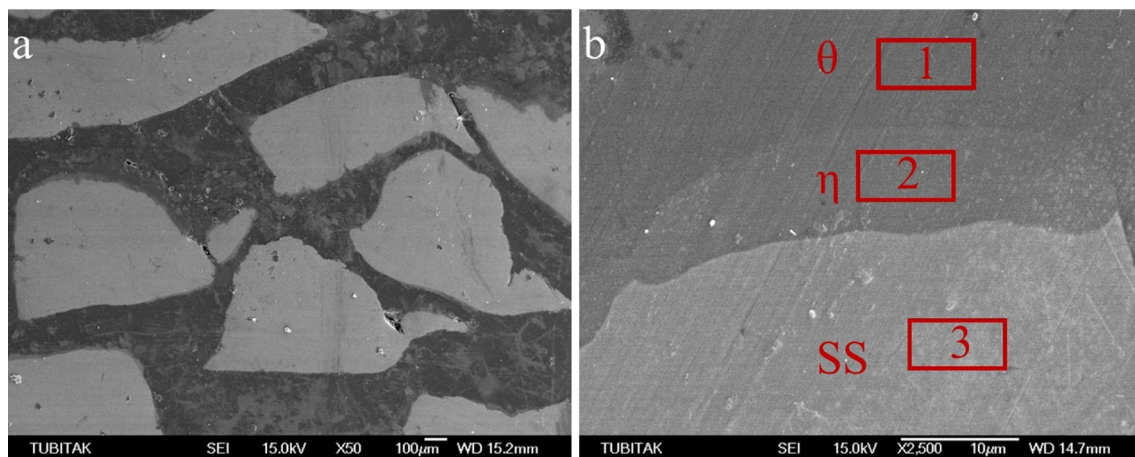
Fig. 5 **a** Low-magnification and **b** high-magnification FEG-SEM images of 30 min preheated 304 SS-reinforced A356 matrix composite

Table 2 Elemental content in wt% of EDS areas in Fig. 5b	Region	Al	Fe	Si	Cr	Ni	C
	1	49.7	18.1	8.4	6.7	–	17.1
	2	46.2	26.0	0.6	9.2	1.6	16.4
	3	–	61.8	–	19.5	6.6	12.1
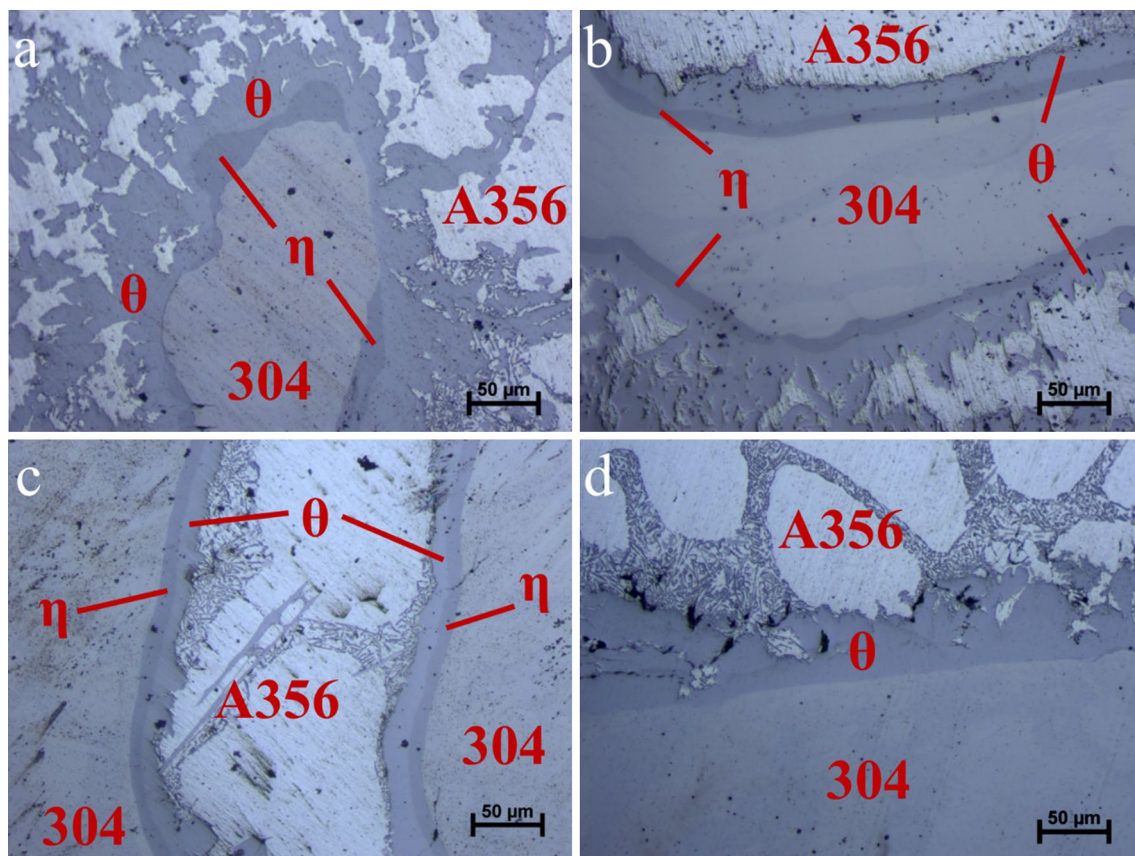
Fig. 6 Microstructures of **a** 0 min, **b** 10 min, **c** 30 min and **d** 60 min preform preheated 304 SS-reinforced A356 matrix composites

According to Fe–Al phase diagram, η formation depends on the peritectic reaction of θ → Liquid + η. When θ formation was restricted by CrO_2 film, η phase automatically cannot be formed. Mentioned CrO_2 film for 60 min preheated specimen should not be confused with CrO_2 peaks in XRD diffractograms indicated in Fig. 4. All samples were covered by limited amount of CrO_2 while waiting after production at room temperature. However, for 60 min preheated sample, CrO_2 film covered SS surface before casting and caused nonformation of η phase. Interfacial phase uniformity of this specimen was also less than that of the others. Locally disrupted zones at θ layer and casting cavities just above the interface are obviously apparent in Fig. 6d. Similarly, non-preheated sample involves few discontinuities in the interfacial region. η layer has not even occurred at some SS/θ interfaces. On the other hand, the uniformity and continuity of θ and η layers of 10 and 30 min preheated specimens seemed quite well.

SEM images with EDS line and related line scanning analysis results of 60 min preheated sample are given in Fig. 7. Analysis direction was from right to the left. Only Cr and O contents were investigated at this part of the characterization to verify microstructural findings. Black zones between A356 and 304 alloys in Fig. 7a indicate CrO_2 film according to line scanning analysis data in Fig. 7b. Cr and O values were only climaxed at this black line during analysis. θ layers existed in remarkable amounts where CrO_2 film did not form. Moreover, some of them were obtained even at the presence of CrO_2. Region that involves EDS analysis line at the left corner of Fig. 7a can be presented as a proof.

3.3 Hardness

Hardness values measured via nanoindentation tester of θ-Fe_4Al_{13} and η-Fe_2Al_5 phases are given as a function of preheating times in Fig. 8. The hardness of θ was reached up to 967 ± 38 HV0.01, whereas the hardness of η was calculated 1184 ± 36 HV0.01 as maximum. Matysik et al. [27] reported that θ-Fe_4Al_{13} hardness varies between 800 and 980 HV in the literature, while η-Fe_2Al_5 hardness varies between 950 and 1100 HV. Although the calculated hardness of θ is in agreement with the previous studies, η hardness is far out of the given range. Even if it was in the range given, the interval was still too wide. This uncertainty on the mechanical properties of these Al-rich intermetallic phases may be the reason for the small interest
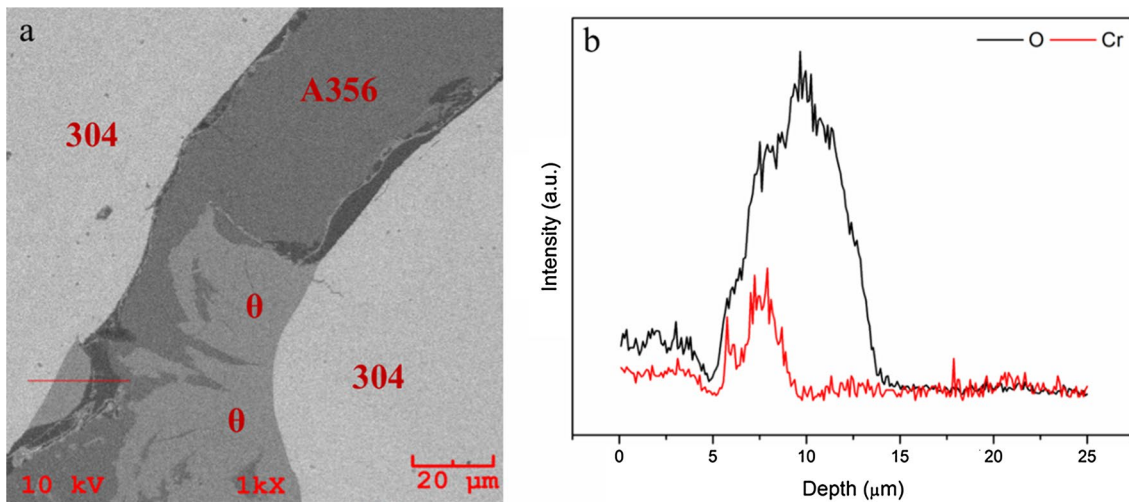
Fig. 7 a SEM images and **b** related EDS line scanning analysis results of 60 min preheated 304 SS-reinforced A356 matrix composite
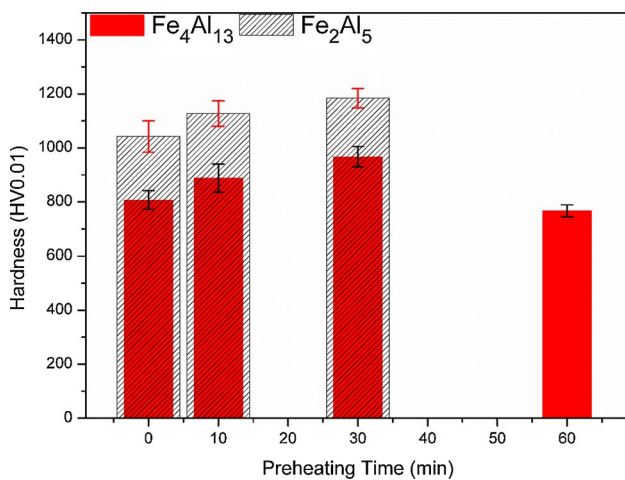
Fig. 8 Hardness results of θ-Fe_4Al_{13} and η-Fe_2Al_5 layers as a function of preform preheating time

on alloys consisting of these phases. On the other hand, it should be noted that the difference in η hardness may be due to the underestimation of the contact area. Depending on the material properties, hardness results can be overestimated in Oliver and Pharr method because of the pileup of material around the contact impression [28].

At first glance in Fig. 8, it seems that the hardnesses of both interfacial layers increase as preform preheating time increases, provided that the results of 60 min preheated sample were ignored. CrO_2 film growth prior to infiltration weakened interface bonding of this specimen as mentioned before. For this reason, both nonformation of η phase and the deterioration of mechanical strength were occurred in this sample.

The main goal of preheating process is to prevent rapid solidification of Al alloy and increase the interaction time between matrix and reinforcement. With increased interaction time by increasing preform preheating time, diffusion of the composite components into interface was enhanced. Diffused Al and Si atoms from Al alloy and Fe, Cr, Ni and C atoms from SS settled into coherent θ or η lattices and caused distortion. Therefore, coherency of the lattices was broken and preexisting internal stress (consequently hardness) was increased.

Although the results are not demonstrated in Fig. 8, hardnesses of A356 matrix and 304 reinforcement were also measured. No alteration was observed in matrix and reinforcement hardnesses as a function of preheating time. According to nanoindentation results, the average hardness of A356 and 304 alloys were calculated 71 ± 7 HV0.01 and 247 ± 16 HV0.01, respectively.

3.4 Worn Surface Examinations

After microstructural evaluation and the hardness determination, composite samples were subjected to wear tests. To determine the influence of 304 reinforcement on wear resistance, monolithic A356 alloy was also abraded under the same test conditions. Low and high-magnification worn surface images taken by SEM are given in Figs. 9 and 10, respectively. It was obviously seen from Fig. 9 that wear track widths of 304 reinforced composites were narrower than that of nonreinforced Al alloy which was affected by different wear mechanisms including abrasion, adhesion, delamination and oxidation. Its worn surfaces involve grooves, plastic flow marks, ridges and craters. It can be readily said that predominant mechanism in nonreinforced sample was adhesion which was
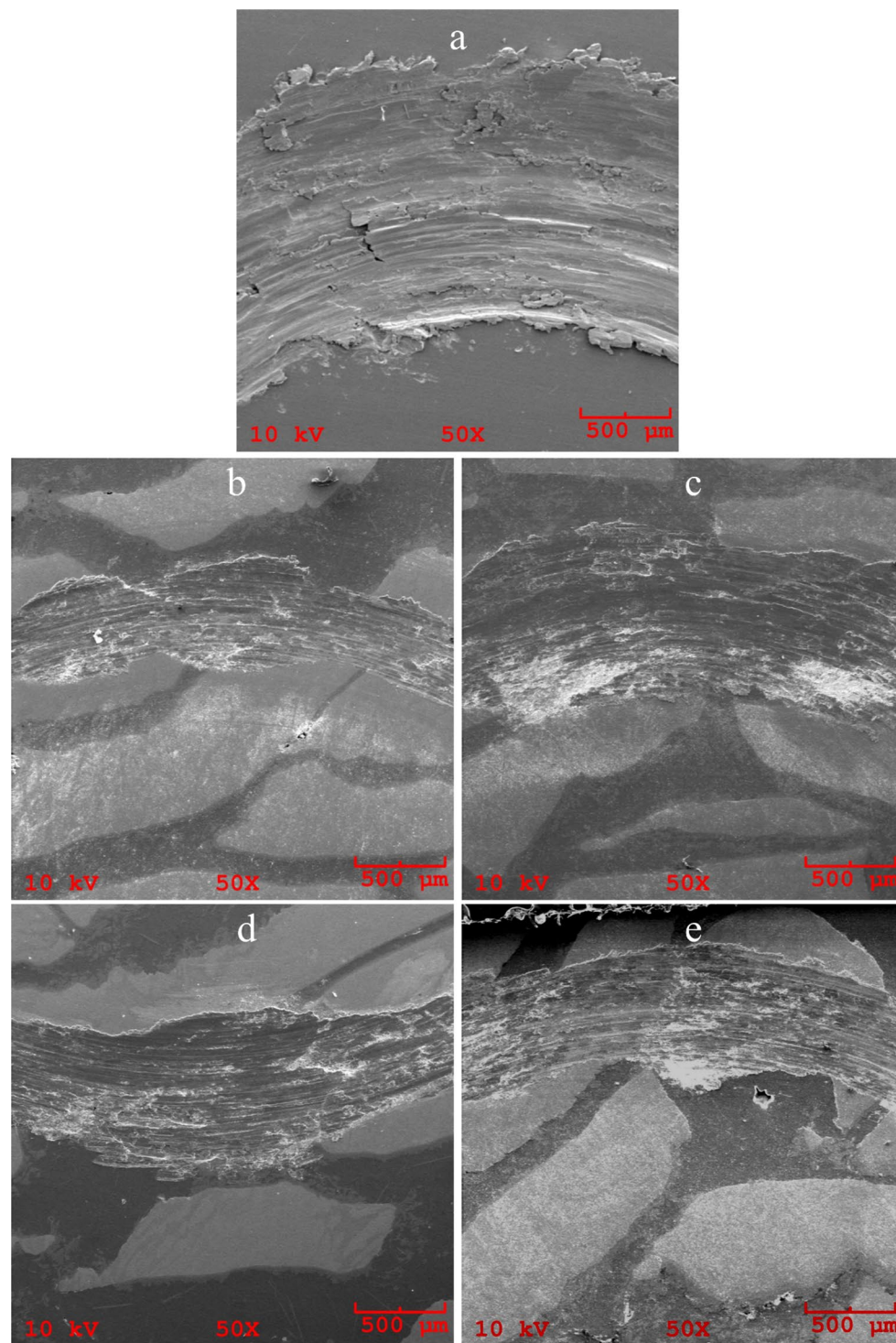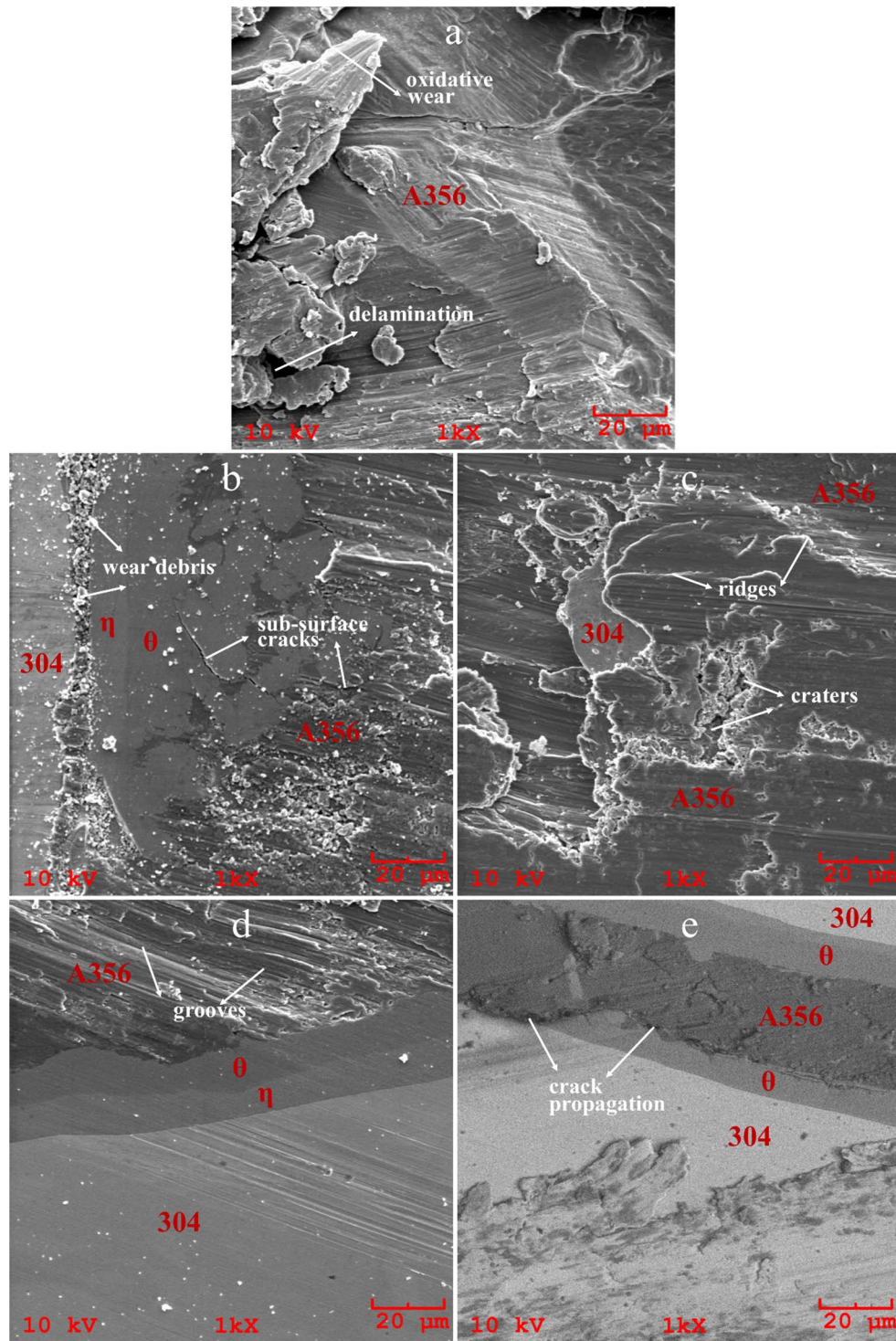
Fig. 9 Low-magnification worn surface images of **a** nonreinforced A356 alloy and **b–e** 304 SS-reinforced A356 matrix composites with **b** 0 min, **c** 10 min, **d** 30 min and **e** 60 min preheating

proved by massive plastic deformation of A356 alloy. Detached Al particles were transferred to Al_2O_3 counterpart during the test and either remained there or participated the matrix again. This transfer cycle was the reason

of ridges and craters which are the evidences of adhesive wear. A small part of the worn surface was covered with narrow grooves parallel to the sliding direction. These grooves indicated that abrasion was also one of the wear

Fig. 10 High-magnification worn surface images of **a** nonreinforced A356 alloy and **b–e** 304 SS-reinforced A356 matrix composites with **b** 0 min, **c** 10 min, **d** 30 min and **e** 60 min preheating

modes involved in wear test of Al alloy. Figure 10a also clearly shows the delamination of Al matrix caused by plastic deformation. From the worn surface images of the monolithic Al phase, the wear resistance was expected to be low under the common effects of so many wear mechanisms.

Some Al zones were locally covered by white thin layers marked in Fig. 10a. This whiteness is a distinctive feature of an oxidation wear. Probably, frictional heating during sliding triggered the oxidation mechanism in nonreinforced A356 alloy. However, oxidation did not affect adversely on wear resistance of Al alloys because of decreased ball-disc contact by oxide film. Moreover, it can be claimed that oxidation wear reduces adhesive wear under dry sliding conditions [29]. SEM images with EDS regions and related EDS results of wear tracks of nonreinforced and reinforced A356 alloy without preheating are given in Fig. 11. It can be surely said that reinforcing A356 matrix with 304 reinforcements dramatically reduced oxidative wear. Before reinforcing, high oxygen content was obtained in wear tracks of monolithic Al alloy, especially at white layer demonstrated in Fig. 11b.

The oxygen amount on white layer was detected at the higher level than anywhere else in wear track. This result was a definite proof that A356 alloy was exposed to oxidation wear locally. After reinforcing, while the oxygen amount in SS-rich region (Fig. 11c) was quite low, it was considerably reduced in Al-rich region (Fig. 11d) compared to nonreinforced Al alloy. It can be inferred that Al part of the composite was responsible for high oxygen content in wear tracks and some of them were plastered on SS side during test.

In general, mostly grooves, ridges and flow marks were obtained in worn surfaces of all composites. These are distinguishing characteristics of abrasion, adhesion and plastic deformation, respectively. There are only a few signs to mention oxidative wear mechanism for
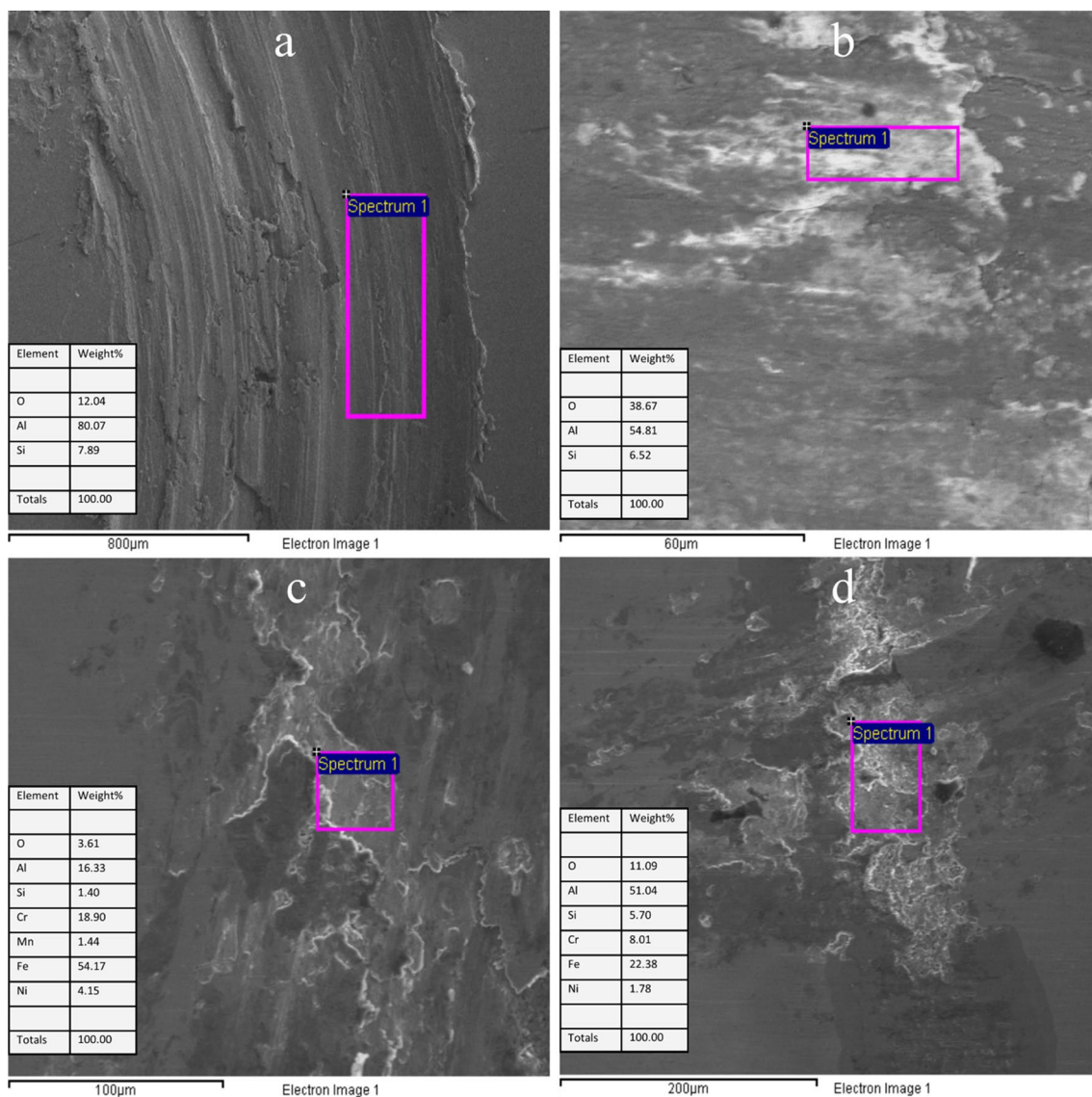
Fig. 11 Wear track analysis of **a**, **b** nonreinforced A356 alloy and **c**, **d** nonpreheated 304 SS-reinforced A356 matrix composite

composites of A356 alloys, according to worn surface images and EDS analysis results.

Subsurface cracks and wear debris of nonpreheated sample are marked in Fig. 10b. The most appropriate sites for crack nucleation are the interfaces between matrix and reinforcement because of high stress concentration [30]. In this specimen, subsurface cracks initiated and propagated by sliding process especially in θ layer formed wear debris by joining together. Particles from cracked layer transferred back and forth during wear test and produce wear debris in the end [31]. Suh [32] offered that wear debris could be formed by delamination which was also observed in Fig. 10b at η/SS interface where debris density was high. Considering worn surface image of 60 min preheated sample (Fig. 10e) that points out crack propagation at θ-Al interface, it can be inferred that these failures may be related to layer hardnesses. Nanoindentation results shown in Fig. 8 show that θ layer hardness of both samples was almost the same and lower than that of other preheated specimens.

Preheating preforms for 10 and 30 min before infiltration provided less severe wear. Ridges and craters noted in Fig. 10c (Al-rich portion) and grooves marked in Fig. 10d (SS-rich portion) expressed that adhesion and abrasion were occurred. These two samples exhibited similar behaviour against wear. θ and η phases acted as barriers to adhesive wear at the beginning of the interface. The predominant mechanism in reinforcement and interface sides was abrasive wear, whereas A356 matrix side was worn under both abrasive and adhesive mechanisms. Similar to nonpreheated and 60 min preheated composites, hardnesses of these specimens were also close to each other. Even significant differences in crystal structures, mechanical strengths or chemical compositions of θ and η did not cause any failure during sliding. It can be concluded from examination of worn surfaces that obtaining θ and η layers with strong bonding led to improve wear resistance. It should not be forgotten that they would cause to multiply wear rate if interface bonding was weak.

In 60 min preheated specimen shown in Fig. 10e, long preheating time caused CrO_2 film formation, instead of η phase. This nonformation of η layer weakened mechanical bonding and due to the repeated ploughing of Al_2O_3 ball during sliding, CrO_2 film was delaminated from Al matrix, together with θ phase. Released oxide asperities participated in wear tracks and caused much more adhesive wear. It should also be noted that crack propagation in this sample was occurred far away from the tribolayer. This distance can be counted as an evidence of the relationship between crack propagation and shear strain generated by sliding.

3.5 Wear Rate and Friction Coefficient

Wear rates were calculated via two different volume loss measurement techniques by both using wear tracks and mass losses. The average results of two methods and standard deviations of the results were given as a logarithmic scale in Fig. 12. Wear rate of nonreinforced A356 alloy was at least ten times higher than that of its composites reinforced with 304 SS. This huge distinction of monolithic Al alloy from its composites was resulted from the dominancy of wear mechanisms. Almost all different wear types acted as a leading role for this sample, while composite structures were abraded under only one or two mechanisms. The best results were attained in 10 and 30 min preheated specimens. Wear resistance of sample not preheated was higher than sample preheated excessively. It was concluded that sufficient preform preheating before casting led to enhance both tribological and mechanical properties by avoiding rapid solidification of Al and consequently increasing solid/liquid interaction time.

Sliding distance-dependent friction coefficients of 304 reinforced A356 composites were given as a function of preheating time in Fig. 13. Friction coefficient values were recorded by tribometer during wear tests perpetually. The minimum results were measured in 10 and 30 min preheated samples. At the first half of sliding, 10 min preheated sample showed better resistance, whereas 30 min preheated sample got ahead against wear at the second half of the test. With increasing sliding distance, 60 min preheated composite began to fail resisting against wear. Probably, this may be resulted from CrO_2 film cracking during sliding.

Hardness results as functions of wear rate and average friction coefficients are given in Fig. 14. Direct relationship between hardness and wear rate is obviously visible in Fig. 14a. With increasing hardnesses of θ-Fe_4Al_{13} and
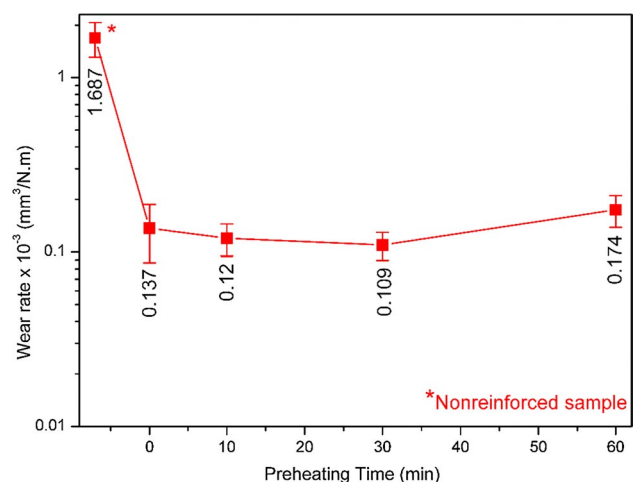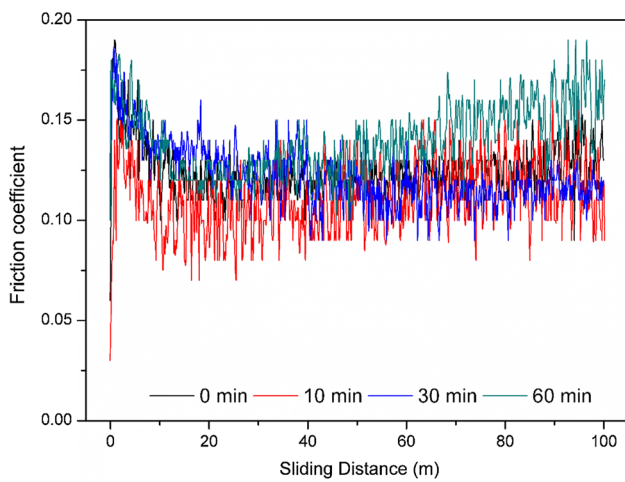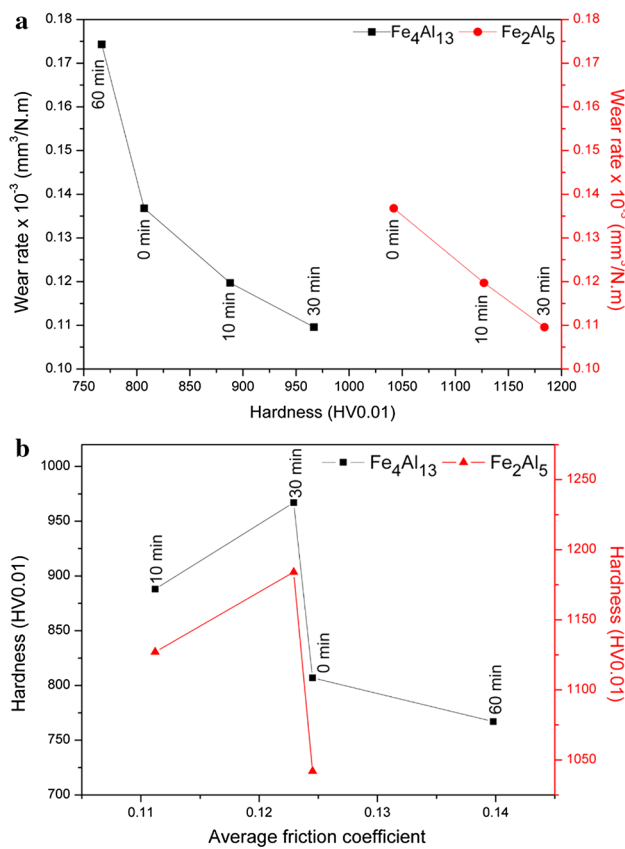

Fig. 12 Wear rate variation as a function of preform preheating time

Fig. 13 Sliding distance-dependent friction coefficients as a function of preheating time

**Fig. 14** Hardness results as functions of **a** wear rate and **b** average friction coefficient

η-Fe_2Al_5 phases, composites behaved more resistant against wear. It was difficult to predict which layer was more responsible for decrease in wear rate because both of them were increasing or decreasing simultaneously. According to

Fig. 14b, nearly same behaviour was observed among hardness and friction coefficient. Average friction coefficient of 10 min preheated sample was calculated higher than that of 30 min preheated one owing to its enormous resistance to wear at the first half of the test. All mechanical and tribological features of these two samples showed similar results, apart from minor differences.
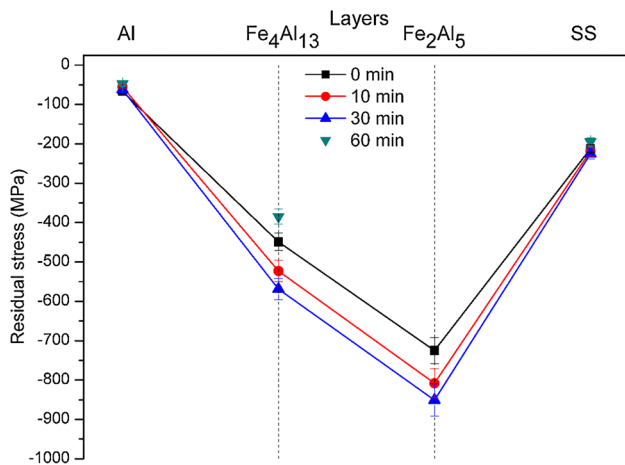
3.6 Residual Stress

Despite the fact that residual stresses have an important influence on wear, corrosion, fatigue and fracture properties of the material, they have been usually ignored at the characterization of the final product. Theoretical and experimental studies [33, 34] showed that residual stresses have enormous effects on load–penetration depth curves recorded by indentation instrument. It is well-known fact that hardness increases with increasing compressive stress and decreases with increasing tensile stress. Figure 15 shows load–depth curves for θ-Fe_4Al_{13} and η-Fe_2Al_5 phases together. It can be seen that compressive residual stress was increased at η phase because more load was required to penetrate η surface at the same indentation depth with θ. In this study, residual stresses were calculated using Wang et al.'s method which was found appropriate as a measurement method with some other techniques in Xiao et al.'s study [35].

Residual stress results derived from load–penetration curves recorded by nanoindentation tester are given in Fig. 16. Average of ten load–depth curves of monolithic A356 cast alloy was admitted as stress-free sample. The internal stresses considerably affect on tribomechanical properties of manufactured metal matrix composites. A356 alloy, as a matrix, should transfer the applied load to the reinforcement without failure. Therefore, it is crucial to
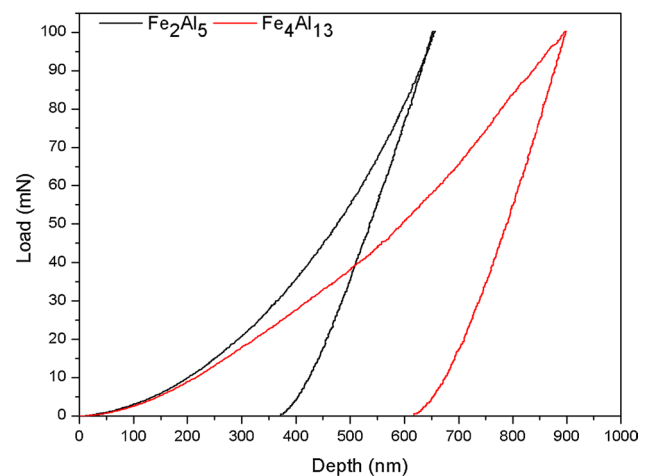
Fig. 15 Load–penetration depth curves of θ-Fe_4Al_{13} and η-Fe_2Al_5 phases

Fig. 16 Residual stress variation inside composites as a function of preheating time

know the extra internal residual stresses caused by the reinforcement and formed reaction phases on Al matrix. Wang et al.'s method seems the most suitable model to point out the beneficial effects of reaction phases individually.

With increasing preform preheating time, compressive residual stress values were increased, except 60 min preheated sample. Compressive stress of θ-Fe_4Al_{13} was reached up to -569 MPa, whereas the maximum stress of η-Fe_2Al_5 was measured -851 MPa. In Al and SS sides, preheating has not any significant effect on the residual stresses. Increased compressive stress makes reaction phases much stronger because it is necessary to apply external pressure at least as far as the internal stress, in order to cause any damage to these phases. Worn surface examinations in Fig. 10 were totally in agreement with residual stress calculations. It should be remembered that in 30 min preheated specimen, double-layered interface with huge compressive stresses blocked the adhesive wear tracks and provided decrease in wear rate.

3.7 Layer Thickness

To determine the relationship between layer thicknesses and tribomechanical properties of produced composites, layer thicknesses were measured by using image analyzer software (Nikon Eclipse MA100). The layer thicknesses of θ and η phases were calculated at ten random points, and the mean results were demonstrated as functions of wear rate and hardness in Fig. 17. It was indirectly seen from Fig. 17 that increasing preheating time provides increased θ thickness, while η thickness was decreased apart from nonpreheated sample. θ thicknesses varied from 18 to 38 µm, whereas η thickness varied between 12 and 16 µm. Ozaki and Kutsuna [36] reported that IMC layer thickness up to 10 µm strengthened Al/SS bonding. If it was less than 10 µm, sample was
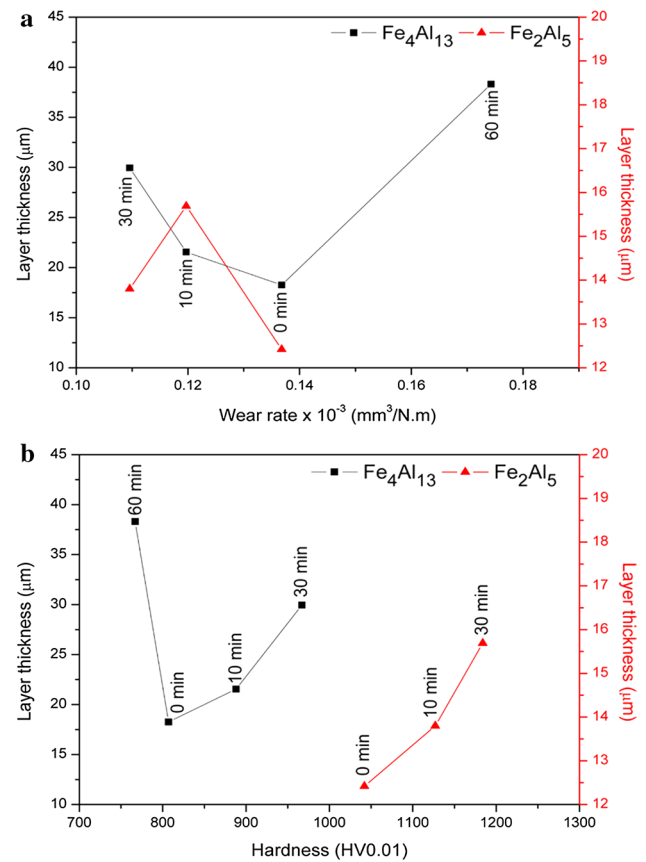
Fig. 17 Layer thicknesses of θ-Fe_4Al_{13} and η-Fe_2Al_5 phases as functions of **a** wear rate and **b** hardness

failed in mechanical strength. Both IMC layers have thicknesses above the critical threshold in this study.

According to Fig. 17a, for 60 min preheated sample, wear rate increased although θ thickness was greater than all others. Except this specimen, wear rate decreased with increasing θ thickness. It seems that nonformation of η decreased the beneficial effect of θ on wear resistance. It is not possible to explain η effect on its own, but it can be definitely said that formation of both phases showed better wear resistance than that of single θ formation. Another proof of this argument was observed in Fig. 17b. Hardness results increased with layer thicknesses, apart from 60 min preheated sample. Non-existence of η caused to decrease in mechanical properties or in other words, formation of η provided increase in mechanical features.

4 Conclusion

304 SS-reinforced A356 alloy matrix composites with several preform preheating times were produced in low-cost environmentally friendly way by using recycled raw materials. θ-Fe_4Al_{13} and η-Fe_2Al_5 phases were formed at

A356/304 interfaces, apart from 60 min preheated specimen. Excessive interaction between preform and oxygen in the furnace caused to form CrO_2 layer on preform surfaces before casting and this oxide film prevented η formation during infiltration.

Reinforcing matrix by 304 SS increased wear resistance 10 times than that of monolithic A356 alloy. Preheating preforms led to increase in hardness, residual stress and wear resistance of composites until preheating time was up to 60 min. In 30 min preheated sample, θ and η hardnesses were reached up to 967 ± 38 and 1184 ± 36 HV0.01, respectively. Along with the common effects of hardness and residual stress, adhesive wear was prevented and only abrasive wear occurred in reinforcement and interface sides. It was understood that perfect combination for better tribo-mechanical properties was preheating preforms between 10 and 30 min.

References

1. Zalensas, D.L.: Aluminum Casting Technology. American Foundry Society (1997)
2. Prasad, S.V., Asthana, R.: Aluminum metal-matrix composites for automotive applications: tribological considerations. Tribol. Lett. **17**, 445–453 (2004). https://doi.org/10.1023/B:TRIL.0000044492.91991.f3
3. Patel, V.K., Bhole, S.D., Chen, D.L., Ni, D.R., Xiao, B.L., Ma, Z.Y.: Solid-state ultrasonic spot welding of SiCp/2009Al composite sheets. Mater. Des. **65**, 489–495 (2015). https://doi.org/10.1016/j.matdes.2014.09.049
4. Chen, S., Teng, J., Luo, H., Wang, Y., Zhang, H.: Hot deformation characteristics and mechanism of PM 8009Al/SiC particle reinforced composites. Mater. Sci. Eng. A **697**, 194–202 (2017). https://doi.org/10.1016/j.msea.2017.05.016
5. Gasem, Z.M., Ali, S.S.: Low-cycle fatigue behavior of powder metallurgy 6061 aluminum alloy reinforced with submicron-scale Al_2O_3 particles. Mater. Sci. Eng. A **562**, 109–117 (2013). https://doi.org/10.1016/j.msea.2012.10.097
6. Rana, H.G., Badheka, V.J., Kumar, A.: Fabrication of Al7075/B4C surface composite by novel friction stir processing (FSP) and investigation on wear. Procedia Technol. **23**, 519–528 (2016). https://doi.org/10.1016/j.protcy.2016.03.058
7. Ravi Kumar, K., Kiran, K., Sreebalaji, V.S.: Micro structural characteristics and mechanical behaviour of aluminium matrix composites reinforced with titanium carbide. J. Alloys Compd. **723**, 795–801 (2017). https://doi.org/10.1016/j.jallcom.2017.06.309
8. Alam, S.N., Kumar, L.: Mechanical properties of aluminium based metal matrix composites reinforced with graphite nanoplatelets. Mater. Sci. Eng. A **667**, 16–32 (2016). https://doi.org/10.1016/j.msea.2016.04.054
9. Landry, K., Kalogeropoulou, S., Eustathopoulos, N.: Wettability of carbon by aluminum and aluminum alloys. Mater. Sci. Eng. A **254**, 99–111 (1998). https://doi.org/10.1016/S0921-5093(98)00759-X
10. Sarkari Khorrami, M., Samadi, S., Janghorban, Z., Movahedi, M.: In-situ aluminum matrix composite produced by friction stir processing using FE particles. Mater. Sci. Eng. A **641**, 380–390 (2015). https://doi.org/10.1016/j.msea.2015.06.071
11. Baron, R., Wert, J., Gerard, D., Wawner, F.: The processing and characterization of sintered metal-reinforced aluminium matrix composites. J. Mater. Sci. **32**, 6435–6445 (1997). https://doi.org/10.1023/A:1018686505563
12. Selvakumar, S., Dinaharan, I., Palanivel, R., Babu, B.G.: Development of stainless steel particulate reinforced AA6082 aluminum matrix composites with enhanced ductility using friction stir processing. Mater. Sci. Eng. A **685**, 317–326 (2017). https://doi.org/10.1016/j.msea.2017.01.022
13. Thangarasu, A., Murugan, N., Dinaharan, I., Vijay, S.J.: Synthesis and characterization of titanium carbide particulate reinforced AA6082 aluminium alloy composites via friction stir processing. Arch. Civ. Mech. Eng. **15**, 324–334 (2015). https://doi.org/10.1016/j.acme.2014.05.010
14. Altinkok, N., Özsert, I., Findik, F.: Dry sliding wear behavior of Al_2O_3/SiC particle reinforced aluminium based MMCs fabricated by stir casting method. Acta Phys. Pol. A **124**, 11–19 (2013). https://doi.org/10.12693/APhysPolA.124.11
15. Tang, L., Gao, C., Huang, J., Zhang, H., Chang, W.: Dry sliding friction and wear behaviour of hardened AISI D2 tool steel with different hardness levels. Tribol. Int. **66**, 165–173 (2013). https://doi.org/10.1016/j.triboint.2013.05.006
16. Lemm, J.D., Warmuth, A.R., Pearson, S.R., Shipway, P.H.: The influence of surface hardness on the fretting wear of steel pairs—its role in debris retention in the contact. Tribol. Int. **81**, 258–266 (2014). https://doi.org/10.1016/j.triboint.2014.09.003
17. Li, J., Lu, Y., Zhang, H., Xin, L.: Effect of grain size and hardness on fretting wear behavior of Inconel 600 alloys. Tribol. Int. **81**, 215–222 (2015). https://doi.org/10.1016/j.triboint.2014.08.005
18. Jeong, D.H., Erb, U., Aust, K.T., Palumbo, G.: The relationship between hardness and abrasive wear resistance of electrodeposited nanocrystalline Ni–P coatings. Scr. Mater. **48**, 1067–1072 (2003). https://doi.org/10.1016/S1359-6462(02)00633-4
19. Allison, J.E., Cole, G.S.: Metal-matrix composites in the automotive industry: opportunities and challenges. JOM **45**, 19–24 (1993). https://doi.org/10.1007/BF03223361
20. Guler, K.A., Kisasoz, A., Karaaslan, A.: Investigation of Al/steel bimetal composite fabrication by vacuum assisted solid mould investment casting. Acta Phys. Pol. A **126**, 1327–1330 (2014). https://doi.org/10.12693/APhysPolA.126.1327
21. Bateni, M.R., Szpunar, J.A., Wang, X., Li, D.Y.: Wear and corrosion wear of medium carbon steel and 304 stainless steel. Wear **260**, 116–122 (2006). https://doi.org/10.1016/j.wear.2004.12.037
22. Quraishi, M.M.: United States Patent (2000)
23. Gecu, R., Atapek, H., Karaaslan, A.: Influence of preform preheating on dry sliding wear behavior of 304 stainless steel reinforced A356 aluminum matrix composite produced by melt infiltration casting. Tribol. Int. **115**, 608–618 (2017). https://doi.org/10.1016/j.triboint.2017.06.040
24. Oliver, W.C., Pharr, G.M.: An Improved Technique for Determining Hardness and Elastic Modulus Using Load and Displacement Sensing Indentation Experiments. http://www.journals.cambridge.org/abstract_S0884291400017039 (1992)
25. Wang, Q., Ozaki, K., Ishikawa, H., Nakano, S., Ogiso, H.: Indentation method to measure the residual stress induced by ion implantation. Nucl. Instrum. Methods Phys. Res. Sect. B Beam Interact. Mater. Atoms **242**, 88–92 (2006). https://doi.org/10.1016/j.nimb.2005.08.008
26. Omori, T., Sato, J., Shinagawa, K., Ohnuma, I., Oikawa, K., Kainuma, R., Ishida, K.: Experimental determination of phase equilibria of Al-rich portion in the Al–Fe binary system. J. Alloys Compd. **668**, 97–106 (2016). https://doi.org/10.1016/j.jallcom.2016.01.215
27. Matysik, P., Józwiak, S., Czujko, T.: Characterization of low-symmetry structures from phase equilibrium of Fe–Al system-microstructures and mechanical properties. Materials **8**, 914–931 (2015). https://doi.org/10.3390/ma8030914

28. Oliver, W.C., Pharr, G.M.: Measurement of hardness and elastic modulus by instrumented indentation: advances in understanding and refinements to methodology. J. Mater. Res. **19**, 3–20 (2004). https://doi.org/10.1557/jmr.2004.19.1.3

29. Ramachandra, M., Radhakrishna, K.: Sliding wear, slurry erosive wear, and corrosive wear of aluminium/SiC composite. Mater. Sci. **24**, 333–349 (2006)

30. Sawla, S., Das, S.: Combined effect of reinforcement and heat treatment on the two body abrasive wear of aluminum alloy and aluminum particle composites. Wear **257**, 555–561 (2004). https://doi.org/10.1016/j.wear.2004.02.001

31. Heilmann, P., Don, J., Sun, T.C., Rigney, D.A., Glaeser, W.A.: Sliding wear and transfer. Wear **91**, 171–190 (1983). https://doi.org/10.1016/0043-1648(83)90252-1

32. Suh, N.P.: The delamination theory of wear. Wear **25**, 111–124 (1973)

33. Tsui, T.Y., Oliver, W.C., Pharr, G.M.: Influences of stress on the measurement of mechanical properties using nanoindentation: part I. Experimental studies in an aluminum alloy. J. Mater. Res. **11**, 752–759 (1996). https://doi.org/10.1557/JMR.1996.0091

34. Bolshakov, A., Oliver, W.C., Pharr, G.M.: Influences of stress on the measurement of mechanical properties using nanoindentation: part II. Finite element simulations. J. Mater. Res. **11**, 760–768 (1996). https://doi.org/10.1557/JMR.1992.0092

35. Xiao, L., Ye, D., Chen, C.: A further study on representative models for calculating the residual stress based on the instrumented indentation technique. Comput. Mater. Sci. **82**, 476–482 (2014). https://doi.org/10.1016/j.commatsci.2013.10.014

36. Ozaki, H., Kutsuna, M.: Laser-roll welding of a dissimilar metal joint of low carbon steel to aluminium alloy using 2 kW fibre laser. Weld. Int. **23**, 345–352 (2009). https://doi.org/10.1080/09507110802542718